Microstructure Characteristics and Melting Behaviors of Smelted Natural Gas-Based Direct Reduced Iron (DRI) with Different Amounts of Biocarbon Addition

GUANG WANG, AYA ZRAIDI, RAHMAN FAIZ SUWANDANA, QING ZHU, SHUJIE YOU, XIANFENG HU, and WANGZHONG MU

Three natural gas-based direct reduced iron (DRI) alloys with varying biocarbon additions were investigated using electron microscopy, thermodynamic calculations, microhardness testing, and high-temperature confocal laser scanning microscope. Increasing carbon content from 2.91 to 5.25 wt pct reduced the complete melting temperature from 1231 to 1174 °C and transformed the microstructure from dendritic ferrite to graphite-rich structures. Oxide particles and impurities formed during remelting and solidification, revealing biocarbon-derived elemental redistribution and providing insights for biocarbon-assisted green steelmaking.

https://doi.org/10.1007/s11663-026-04304-9
© The Author(s) 2026

NOWADAYS, the DRI shaft furnace (SF)–electric smelting furnace (ESF)–basic oxygen furnace (BOF) route has attracted increasing attention for low-carbon steel production due to its compatibility with existing integrated steelmaking infrastructure and flexibility in raw material handling.[1–5] Recent studies have demonstrated that carbon addition, gangue characteristics, and carburization behavior strongly influence the melting and slag-metal reactions of DRI/HBI (hot briquetted iron) during electric smelting processes.[6–12] However, these studies have mainly focused on the melting behavior of DRI, carburization mechanisms, and the influence of gangue or slag chemistry, while the subsequent remelting kinetics of DRI-derived metallic alloys remains less explored.

However, the carbon content in hot metal produced from commercial direct reduced iron (typically C < 4 wt pct)[13] in ESF is often insufficient for subsequent BOF operation (> 3 wt pct C in hot metal),[12] requiring additional carbon introduction during smelting.[12,14–16] Biocarbon has recently attracted interest as a sustainable carbon source[17–20]; however, its addition not only changes the total carbon content but may also influence carbon bonding states, microstructure evolution, and impurity redistribution during high-temperature processing.

In this study, three alloys (samples) were produced by smelting natural gas-based direct reduced iron (DRI) with slag former and biocarbon addition. Carbon content strongly influences the melting behavior of Fe-based alloys, including liquid formation, phase evolution, and carbon redistribution during remelting.[7,21,22] Nevertheless, the relationship between carbon content, microstructural characteristics, and remelting behavior of DRI-derived alloys produced with biocarbon remains insufficiently understood, particularly under dynamic high-temperature conditions. Therefore, the present work investigates the melting behavior of samples with different carbon contents produced using DRI with *via* high-temperature confocal laser scanning microscopy (HT-CLSM), with particular focus on melting temperature, microstructure evolution, and carbon redistribution behavior during remelting.

The samples were produced by smelting around 50 g DRI in an MgO crucible at 1600 °C with a holding time of 30 minutes under N_2 atmosphere *via* resistance heating furnace. Before smelting, slag former consisting of 37.6SiO_2-14.6Al_2O_3-38.2CaO-9.7MgO (wt pct), and biocarbon particle (91 wt pct C, 8 wt pct volatile and 1 wt pct moisture) were added to dissolve the gangues and recarburize the metal samples, respectively. The Cu tracer added during DRI smelting. This smelting procedure was designed to simulate real practice in ESF. The chemical compositions of the DRI and three samples are listed in Tables I and II, respectively. An HT-CLSM (VL2000DX-SVF17SP, Yonekura), as presented in supplementary Figure S1, was used to investigate the melting behavior of the samples at the sample/Ar interface through continuous *in situ* observation. Detailed information

GUANG WANG, AYA ZRAIDI, RAHMAN FAIZ SUWANDANA, and SHUJIE YOU are with the Division of Materials Science, Department of Engineering Science and Mathematics, Luleå University of Technology, 97187, Luleå, Sweden. QING ZHU is with the Division of Materials Science, Department of Engineering Science and Mathematics, Luleå University of Technology and also with the Key Laboratory of Electromagnetic Processing of Materials (Ministry of Education), School of Metallurgy, Northeastern University, Shenyang 110819, Liaoning, P.R. China. XIANFENG HU is with the Swerim AB, Box 812, 97125, Luleå, Sweden. WANGZHONG MU is with the Division of Materials Science, Department of Engineering Science and Mathematics, Luleå University of Technology and also with the Wallenberg Initiative Materials Science for Sustainability, Department of Engineering Science and Mathematics, Luleå University of Technology, 97187, Luleå, Sweden. Contact email: wangzhong.mu@ltu.se

Manuscript submitted July 29, 2026; accepted September 9, 2026.

Published online: 02 October 2026

regarding sample preparation, HT-CLSM operation procedures, chemical composition and phase analysis, microstructural characterization, and hardness measurements before and after experiments refer to online supplementary material.

In addition, thermodynamic calculations were performed using FactSage 8.4 with the FToxide and FSstel databases. The phase evolution of the three samples was simulated over the temperature range of 700 to 1350 °C. The maximum temperature 1350 °C was employed to ensure that all samples can be fully melted under this temperature.

Figure 1 presents the thermodynamical simulation results regarding the phase evolution of the three samples from 700 to 1350 °C at 1 atm under Ar atmosphere. As can be seen that the phase transition temperature (T_1) from BCC to FCC was calculated to be 727 °C for sample 1 and sample 2, and 724 °C for sample 3. The onset temperature for liquid phase formation (T_2) was identical for all three samples at 1133 °C. However, the complete phase transformation temperature from FCC to liquid (T_3) significantly decreased from 1246 to 1156 °C as the carbon content increased from 2.91 to 4.21 wt pct, which is attributed to the increased formation of cementite and the corresponding depression of the melting temperature in the Fe-C system. Since higher carbon levels promote eutectic liquid formation and lower the melting temperature. A further increase in carbon content to 5.25 wt pct did not lead to an additional reduction in T_3. Instead, excess carbon remained to be undissolved and was present as graphite in sample 3.

Figure 2(a) depicts the XRD pattern of the DRI pellets used for samples production. The main phases are iron (Fe), cementite (Fe_3C) and graphite metal carbides (Fe_2C_{12}), together with residual FeO and gangue phases identified as $Ca(Fe, Mg)(SiO_3)_2$. The XRD patterns for the three samples are presented in Figure 2(b). Compared with the DRI pellet, the gangue phase disappeared in all samples, suggesting effective slag-metal separation during smelting. FeO and Fe_2C_{12} phase were still detected in the samples, while Fe_7C_3 phase formed instead of Fe_3C phase after smelting and carburization. Spinel ($MgAl_2O_4$) phase was only measured in sample 1, whereas C (graphite) peaks were observed in sample 2 and sample 3. This difference is associated with the production conditions of the samples. sample 1 was produced without biocarbon and slag former addition, while sample 2 and sample 3 were prepared with the addition of slag former and 1.3 and 2.6 g biocarbon, respectively. The results indicate that slag former addition promoted slag separation, while biocarbon addition enhanced carburization of the liquid sample. These results indicate that the alternative way for sustainable utilization of low grade DRI to produce green hot metal.

Figure 3 shows the optical microscopy images of the samples with different carbon contents at magnifications of 25×, 100×, and 200×. Significant microstructural changes

Table I. The Chemical Composition of DRI, Wt Pct

C	Fe	FeO	SiO_2	Al_2O_3	CaO	MgO	ZnO	P	S
3.64	82.55	6.18	4.10	1.53	1.26	0.70	0.03	0.01	0.01

Table II. The Chemical Composition of the Three Samples

	Mn	Cu	C	Si	O	S	Fe	Note
Sample 1	0.2	2.0	2.91	0.7	0.32	0.006	bal.	no additions
Sample 2	0.2	1.2	4.21	0.3	0.11	0.001	bal.	slag former + 1.3 g biocarbon
Sample 3	0.2	1.2	5.25	0.2	0.04	0.001	bal.	slag former + 2.6 g biocarbon

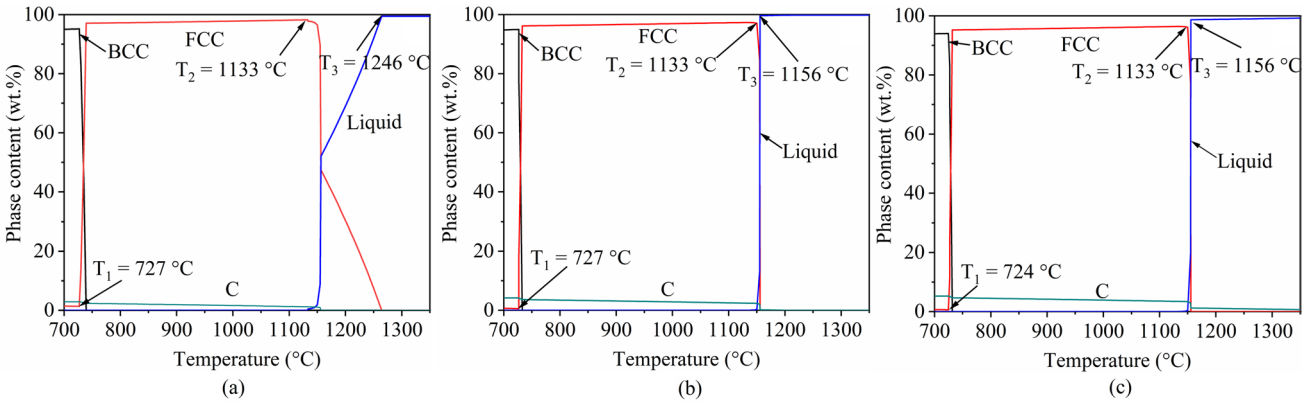

Fig. 1—The equilibrium phases evolution as a function of temperature for the samples, (*a*) through (*c*) corresponding sample 1 to sample 3, respectively. T_1 and T_2 donate phase transformation temperature from BCC to FCC and FCC to liquid, and T_3 is complete phase transformation temperature from FCC to liquid of the samples.

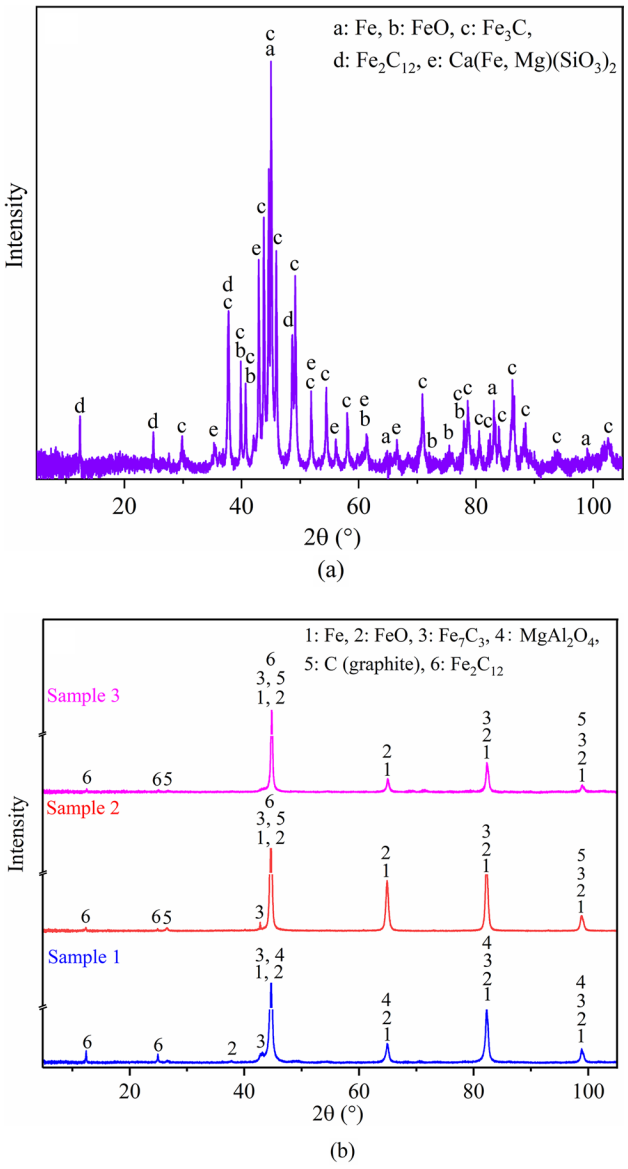

Fig. 2—The XRD patterns for (*a*) the DRI pellet and (*b*) sample 1, 2 and 3 at room temperature.

were observed with increasing carbon content from 2.91 to 5.25 wt pct.

Sample 1 with 2.91 wt pct C exhibited a coarse hypoeutectic structure dominated by large and continuous primary dendrites (light regions). During solidification, these iron-rich dendrites continuously rejected carbon into the liquid, restricting the gray eutectic phase to narrow intercellular networks [Figures 3(a) through (c)]. With increasing carbon content to 4.21 wt pct in sample 2, the coarse dendritic network collapses, refining into a highly uniform, isotropic mesh of fine eutectic phases and, curved graphite flakes [Figures 3(e) through (g)]. This minimization of phase scale is governed by a coupled, cooperative eutectic growth mechanism operating under a drastically reduced melting range (T_3–T_2) predicted by thermodynamic calculations (Figure 1). For sample 3 (5.25 wt pct C) as shown in Figures 3(h) through (j), coarse plate-like and needle-shaped dark phases were observed throughout the matrix, corresponding to graphite phase formed due to the high amount of biocarbon addition. The heterogeneous microstructure agrees well with the thermodynamic simulation and XRD results, which indicated saturation of carbon in sample 3. Overall, the increasing carbon content promoted eutectic formation, refined the matrix structure, and eventually resulted in the precipitation of graphite phases in the high-carbon content samples.

Figure 4 presents the EBSD characterization and carbon EDS mapping results of the three samples. The EBSD phase maps reveal that ferrite is the predominant matrix phase in all three samples, while graphite is the major carbon-containing secondary phase, with only a minor amount of cementite detected. When there is no biocarbon addition (sample 1 with 2.91 wt pct C), the graphite is mainly present as discontinuous carbon-rich regions. The corresponding C elemental map shows localized carbon enrichment, indicating limited graphite precipitation without biocarbon addition. With increasing biocarbon addition to 1.3 g (sample 2 with 4.21 wt pct C), the graphite phase becomes more abundant and tends to form small plate-like structure. This is consistent with a higher carbon enrichment level observed in the carbon elemental map (indicated by the arrows in Figure 4(b_4). When the biocarbon addition is further increased to 2.6 g (sample 3 with 5.25 wt pct C), coarse flake-like and relatively large plate-like graphite is clearly observed. This corresponds to the regions of marked carbon enrichment shown in the carbon elemental map [Figure 4(c_4)], demonstrating significant graphite segregation. The inverse pole figure (IPF) maps suggest that the ferrite matrix exhibits a relatively large grain morphology without biocarbon addition, whereas adding biocarbon leads to a more fragmented ferrite grain structure, likely due to the increased precipitation and segregation of graphite.

The localized Vickers microhardness (HV0.1) test was carried out on the gray and light regions shown in Figure 3. The average hardness values at gray and light regions for samples 1 to 3 are 114 ± 3 and 293 ± 16, 146 ± 7 and 250 ± 4, 132 ± 10 and 276 ± 38, HV0.1, respectively. Combined with microstructural observations (Figure 3) and EBSD results (Figure 4), the lower hardness is consistent with ferritic dendritic/interdendritic regions containing fine eutectic graphite, whereas the higher hardness of the white regions supports their identification as ferritic regions without graphite precipitation.

Figure 5 presents the SEM images of the three samples before and after the *in situ* observation experiments at different magnifications. Before heating, sample 1 with 2.91 wt pct C [Figures 5(a_1) through (a_2)] mainly consists of ferrite (light regions), surrounded by a darker, continuous network of intercellular eutectic phases. With increasing carbon content to 4.21 wt pct in sample 2, the ferrite dendrite arms became significantly finer, while graphite-rich phases became the dominant and more homogeneously distributed phase throughout the matrix [Figures 5(b_1) through (b_2)]. This refinement is attributed to the decrease in the theoretical melting range (T_3–T_2, Figure 1) from 113 °C for sample 1 to 33 °C for sample 2, which shortened the solidification time and restricted dendritic growth.

Further increasing the carbon content to 5.25 wt pct resulted in the formation of needle- and plate-like graphite phases in sample 3 [Figures 5(c_1) through (c_2)]. The addition

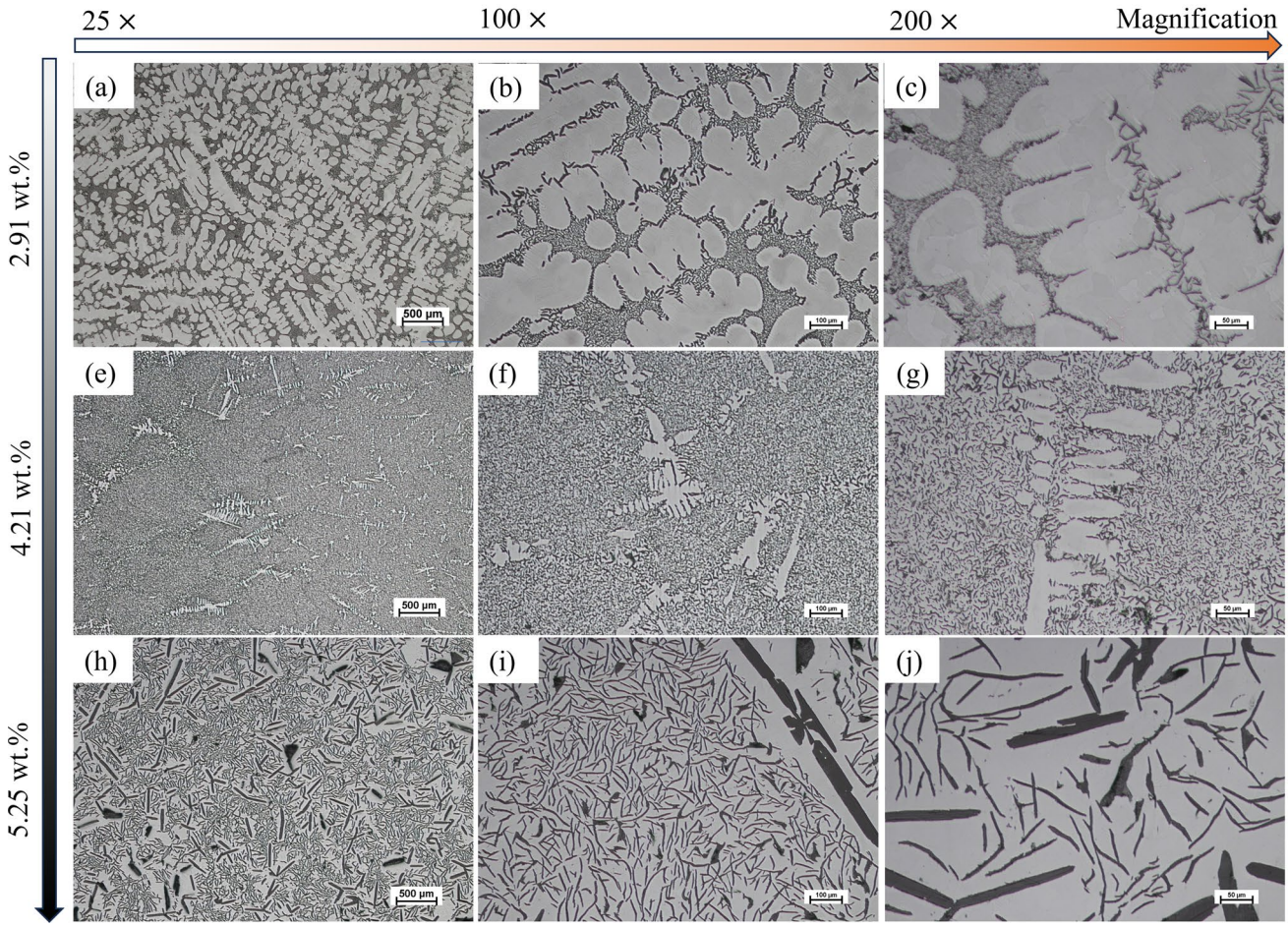

Fig. 3—Optical microscopy images for the three samples at different magnification, (*a*) through (*c*) for sample 1, (*e*) through (*g*) for sample 2, and (*h*) through (*j*) for sample 3.

of biocarbon initially promoted the transformation of ferrite into graphite-rich phases. However, high amount biocarbon addition led to local carbon supersaturation in the liquid sample 3, causing excess carbon to precipitate as graphite during solidification. These observations are consistent with the thermodynamic simulation results (Figure 1), XRD and OM image analysis (Figures 2, 3), and the carbon elemental map results (Figure 4).

Figures 5(a_3) and (a_4), (b_3) and (b_4), and (c_3) and (c_4) illustrates the surface morphologies following the high-temperature *in situ* observation experiments, revealing a pronounced accumulation of graphite-rich phases across all alloy surfaces. This graphite coverage scales directly with the initial carbon content; while sample 1 exhibits localized matrix distortion, the surfaces of samples 2 and 3 become nearly fully blanketed by highly continuous, flake-like graphite structures. This extensive surface coverage highlights the accelerated thermal degradation and phase decomposition taking place along the high-energy eutectic networks and primary carbon channels during thermal exposure.

SEM-EDS characterization was performed to detect the chemical composition of regions with different scales observed in Figures 5(a_3) and (a_4), (b_3) and (b_4), and (c_3) and (c_4) as well as sample 1 before *in situ* experiment, and the results are presented in Figure 6. Prior to the melting, sample 1 contained complex inclusions composed of MnS with embedded Al_2O_3 particles, as shown in Figure 6(a). Graphite in form of sphere and needle were also detected, and it is noteworthy that spherical graphite was partially surrounded by a SiO_2 phase. In addition, P enriched at the interface between the MnS inclusion and the graphite particle. Deep analysis of P behavior during the carburizing process using biocarbon in DRI will be quantitative analyzed in future work.

After the *in situ* observation experiments, numerous nano-sized MnO particles formed in sample 1 [Figure 6(b)], whereas larger MnO particles with lower number density were observed in sample 2 and sample 3 [Figures 6(d) and (e)]. This difference suggests that the carbon content might also affect the redistribution of Mn-containing phases during melting.[23] In addition, rosette-like KCl phase was identified in sample 2 [Figure 6(c)] and were absent in both sample 1 and sample 3. The KCl phase is believed to originate from impurities introduced by the biocarbon and became locally concentrated during melting. This observation highlights the importance of stringent control over the carbon source and its impurity content to minimize the formation of undesirable secondary phases in the samples during melting. From an industrial perspective, the presence and redistribution of impurity-containing phases, such as MnO and KCl, may influence

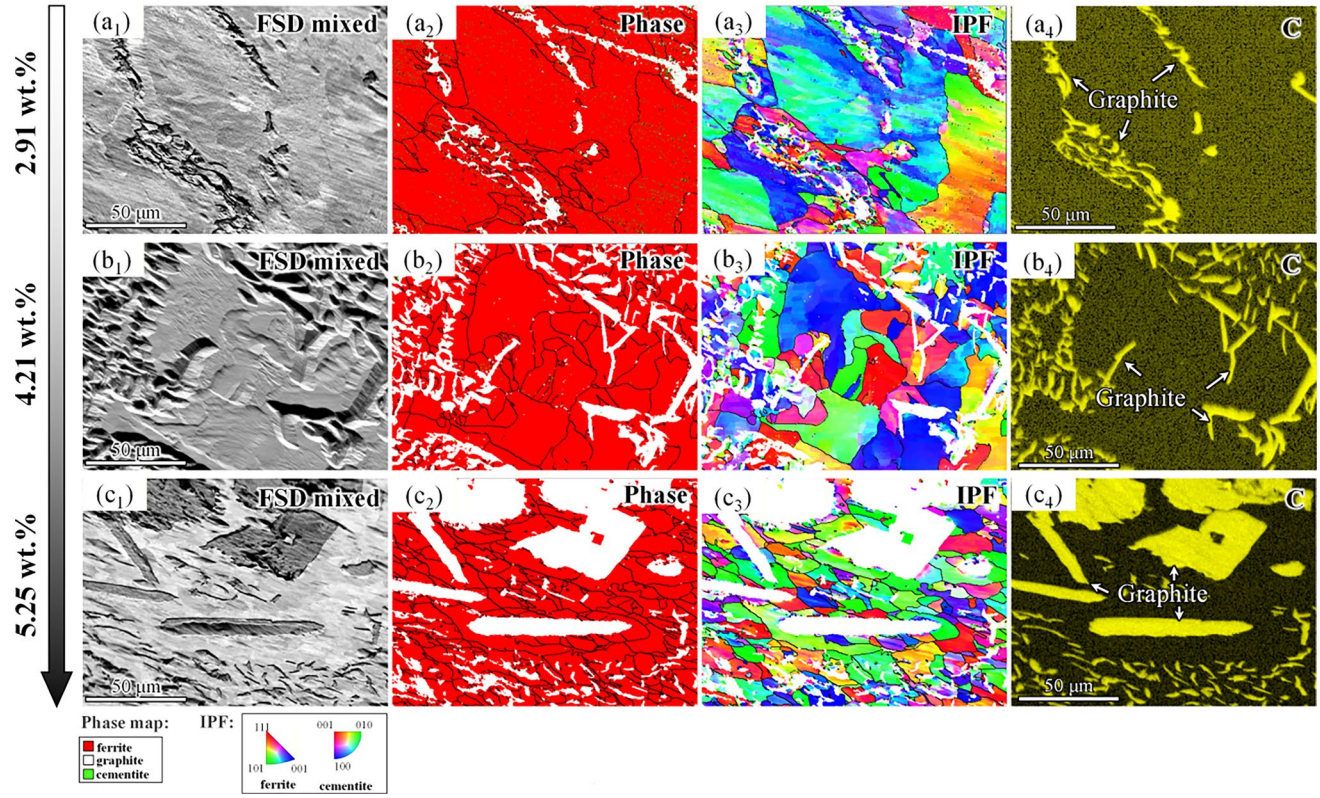

Fig. 4—EBSD phase maps, inverse pole figures (IPF), and carbon energy dispersive spectroscopy (EDS) patterns. (a_1) through (a_4) for sample 1, (b_1) through (b_4) for sample 2, and (c_1) through (c_4) for sample 3.

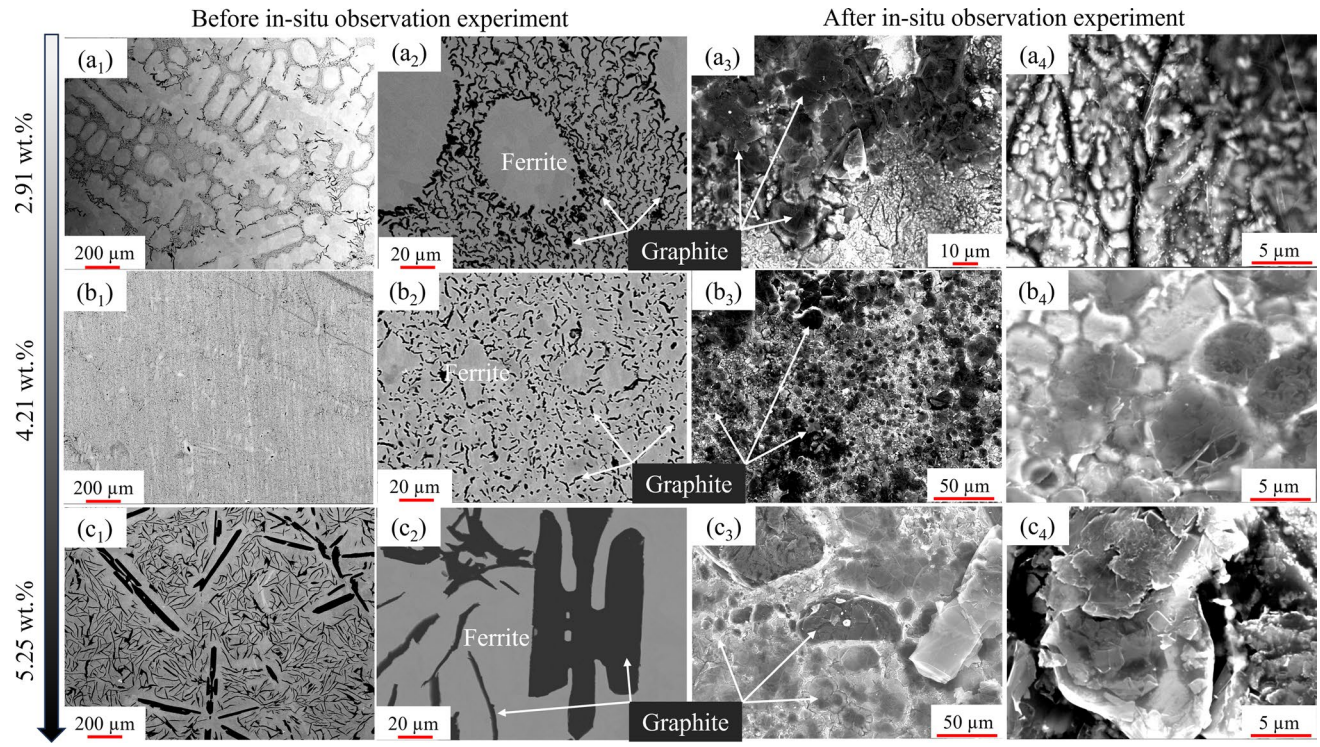

Fig. 5—SEM image for samples before (i_1 and i_2) and after (i_3 and i_4) *in situ* observation experiments at different magnifications. i = a, b, c.

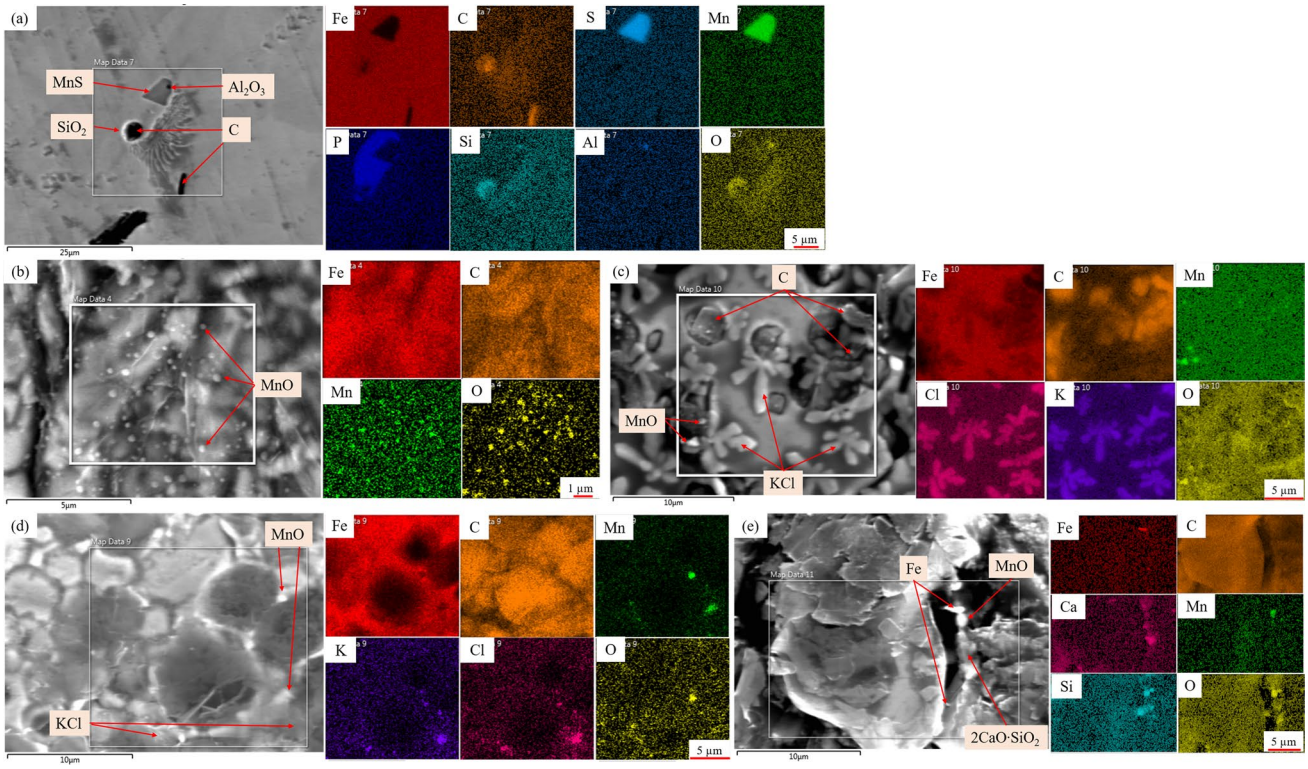

Fig. 6—SEM-EDS results for (*a*) sample 1 before *in situ* experiment, (*b*) for sample 1, (*c*) and (*d*) for sample 2 and (*e*) for sample 3 after *in situ* experiments.

slag chemistry, inclusion behavior, and potentially refractory interactions during electric smelting operations.[24–26] Therefore, controlling the impurity levels in biocarbon is essential for improving process stability and achieving consistent metal quality. In sample 3, a CaO-SiO_2 phase was detected at the edge of flake graphite [Figure 6(e)]. Overall, the SEM-EDS results demonstrate that biocarbon additions significantly influenced graphite precipitation, oxide evolution, and inclusion redistribution in the samples during melting.

Figure 7 presents the *in situ* HT-CLSM observations results of the phase transition, melting, and solidification of the samples under Ar atmosphere. During heating, the ferrite (BCC) to austenite (FCC) transformation initiated at 741, 749, and 720 °C and completed at 838, 821, and 800 °C for sample 1 to sample 3, respectively [Figures 7(a_1) through (a_3) and (b_1) through (b_3)]. It is found that increasing the carbon content from 2.91 to 5.25 wt pct reduced the BCC to FCC transformation temperature range from 97 to 67 °C, indicating that higher carbon content accelerated the phase transition. The first liquid phase appeared at 1132 °C for all samples [Figures 7(c_1) through (c_3)], which agrees well with the thermodynamic simulation results shown in Figure 1. However, the temperature required to completely melt the FCC phase within the observation area decreased significantly from 1231 °C for sample 1 to 1174 °C for sample 3 [Figures 7(d_1) through (d_3)]. This behavior confirms that increasing carbon content promoted liquid formation and reduced the melting temperature of the samples.

During melting, irregular-shaped solid phases [dark contrast Figures 7(d_1) and (d_2)] were observed floating on the liquid metal surface in sample 1 and sample 2. These phases are mainly attributed to carbon-rich phases re-precipitated during cooling rather than residual undissolved graphite, as the thermodynamic calculations (Figure 1) indicate that the carbon content in these alloys remains below the graphite saturation limit during melting. In contrast, flake- and needle-shaped solid phases were detected on the liquid surface of sample 3 [Figure 7(d_3)], which are considered to be a combination of partially undissolved graphite during remelting and newly re-precipitated graphite during cooling, resulting from the excess carbon content exceeding the solubility limit of the liquid alloy. Figures 7(e_1) through (e_3) and (f_1) through (f_3) show the progressive graphite enrichment during the solidification process. Graphite-rich phases gradually precipitated and accumulated on the liquid surface during cooling, particularly in sample 2 and sample 3. This behavior is consistent with the post-experimental SEM-EDS observations (Figures 5, 6), where a graphite-rich surface layer was detected after the *in situ* experiments.

In addition, the variation in melting behaviors with increasing carbon content is closely related to the carbon bonding state in the samples. In sample 1, carbon mainly existed in cementite phase, resulting in a relatively wide melting range. Increasing carbon content promoted the formation of eutectic, graphitic metal carbides, and cementite-containing phases in sample 2, which enhanced liquid formation and reduced the liquidus temperature. In contrast, further biocarbon addition in sample 3 exceeded the carbon solubility limit (4.29 wt pct at 1250 °C), leading to the precipitation of graphite phases. Compared with dissolved or carbide-bound carbon, graphitic carbon contributed less effectively to melting point depression and remained partially undissolved during remelting. These results suggest that both

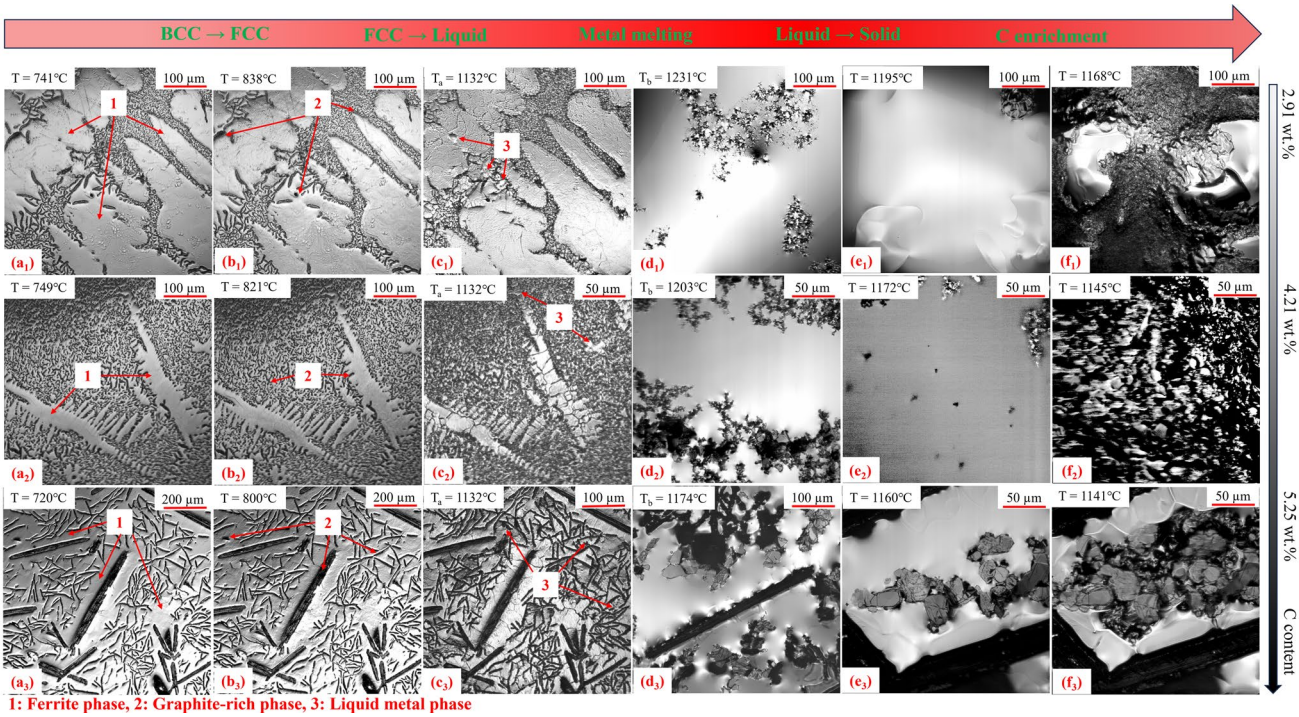

Fig. 7—*In situ* images showing the heating, melting and cooling process for samples under Ar atmosphere, (a_1) through (f_1) for sample 1, (a_2) through (f_2) for sample 2, and (a_3) through (f_3) for sample 3.

carbon content and carbon bonding state strongly influence the phase evolution and melting behavior of the samples.

Moreover, the carbon content also significantly affected the melting range (ΔT) of the three samples, based on the thermodynamic calculations (Figure 1, $\Delta T = T_3 - T_2$) and *in situ* HT-CLSM observations (Figure 7, $\Delta T = T_b - T_a$). According to the thermodynamic simulation and experimental results, ΔT decreased significantly from 113 to 23 °C, and 99 to 42 °C with increasing carbon content from 2.91 to 5.25 wt pct, respectively, due to the reduction in liquidus temperature, indicating that higher carbon content promoted liquid formation and accelerated the melting process. The discrepancy between the thermodynamic and experimental results is likely associated with carbon segregation and graphite precipitation during heating, which are not fully considered in equilibrium calculations. The narrower melting range observed in the samples is beneficial for industrial smelting operations, as it can reduce energy consumption and shorten the melting time, thereby improving the process productivity and supporting green steel production.

In this work, the remelting behavior of three samples produced from DRI with different biocarbon additions was investigated using HT-CLSM, thermodynamic simulations, and microstructural characterization and microhardness test. Increasing carbon content from 2.91 to 5.25 wt pct lowered the liquidus temperature and narrowed the melting range, while the T_a remained nearly unchanged at ~ 1132 °C. The T_b decreased from 1231 to 1174 °C with increasing carbon content, indicating enhanced melting behavior.

Microstructural evolution from ferrite structures to graphite-rich phases was observed with increasing biocarbon addition. Graphite-like phases, oxide particles, and other impurities were detected after remelting, suggesting carbon enrichment and impurity redistribution during heating and cooling. The results demonstrate that carbon content strongly influences the phase evolution, grain size, and melting behavior of samples, providing insights for the sustainable utilization of DRI in environmentally friendly route.

ACKNOWLEDGMENTS

G. Wang & W. Mu would like to acknowledge Kempestiftelserna (JCSMK25-0079) to support this research. Wallenberg Initiative Materials Science for Sustainability (WISE) and Jernkontoret and the Knut and Alice Wallenberg Foundation are also acknowledged. X. Hu would like to acknowledge the support from the Center of Advanced Mining and Metallurgy (CAMM) at the Luleå University of Technology, Sweden.

FUNDING

Open access funding provided by Lulea University of Technology.

CONFLICT OF INTEREST

The authors declare no conflicts of interest.

OPEN ACCESS

This article is licensed under a Creative Commons Attribution 4.0 International License, which permits use, sharing, adaptation, distribution and reproduction in any medium or format, as long as you give appropriate credit to the original author(s) and the source, provide a link to the Creative Commons licence, and indicate if changes were made. The images or other third party material in this article are included in the article's Creative Commons licence, unless indicated otherwise in a credit line to the material. If material is not included in the article's Creative Commons licence and your intended use is not permitted by statutory regulation or exceeds the permitted use, you will need to obtain permission directly from the copyright holder. To view a copy of this licence, visit http://creativecommons.org/licenses/by/4.0/.

SUPPLEMENTARY INFORMATION

The online version contains supplementary material available at https://doi.org/10.1007/s11663-026-04304-9.

REFERENCES

1. G. Sa, W. Ezra, S. Takshi, C.Kyle, W. Christopher, and C. Ian: *AISTech 2023—The Iron & Steel Technology Conference and Exposition*, AISTech, Detroit, 2023, pp. 508-18.
2. P. Khadijeh, G. Craig, and H. Thomas: *International Congress on Science and Technology of Ironmaking*, Metallurgical Industry Press, Beijing, China, 2025, pp. 1232-37.
3. J.M. Margutti, M. Schiedeck, M. Philipp, D. Sarah, K. Sabrine, W. Thomas, and P. Andreas: *Int. J. Hydrogen Energy*, 2026, vol. 235, pp. 155073–86.
4. S. Shabnam, K. Ujwal, B. Geoffrey, R. Ma, O. Kwaku, K. Banty, C. Chunlin, and G. Adrien: *J. Sust. Metall.*, 2026, vol. 9, pp. 1–14.
5. L.Z. Yang, Z. Feng, H. Hu, G.S. Wei, B.T. Xue, Y.F. Guo, and T. Jiang: *J. Iron. Steel Res. Int.*, 2025, vol. 32, pp. 485–518.
6. B. Voraberger, G. Wimmer, A. Pfeiffer, K. Pastucha, and R. Millner: *Metall. Res. Technol.*, 2026, vol. 123, p. 15.
7. A. Pfeiffer, G. Wimmer, and J. Schenk: *Materials*, 2022, vol. 15, p. 5691.
8. C. Garlick, T. Singh, K. Paymooni, D. O'Dea, and T. Honeyands: *J. Sust. Metall.*, 2025, vol. 12, pp. 1114–27.
9. C. DiGiovanni and T. Echterhof: *J. Sust. Metall.*, 2024, vol. 10, pp. 2047–67.
10. M.J. Lee and J.H. Park: *Metall. Mater. Trans. B*, 2026, vol. 57B, pp. 2792–2805.
11. H. Pousette, N. Kojola, and O. Hessling: *Metall. Mater. Trans. B*, 2024, vol. 55B, pp. 4257–70.
12. J.S. Bae and J.H. Park: *J. Clean. Prod.*, 2025, vol. 524, pp. 146490–214500.
13. K. Geonu, K. Yilmaz, and P.P. Christiaan: *Metall. Mater. Trans. B*, 2019, vol. 50B, pp. 2508–16.
14. J.P. Birat: *Mater. Tech.*, 2023, vol. 111, pp. 201–18.
15. W. Gerald, V. Bernhard, K. Benjamin, and F. Alexander: *Mitsubishi Heavy Ind. Tech. Rev.*, 2022, vol. 59, pp. 1–7.
16. Y.L. Zhang: *Steel Times Int.*, 2023, vol. 47, pp. 52–55.
17. S.E. Ibitoye, C. Loha, R.M. Mahamood, T.C. Jen, M. Alam, I. Sarkar, P. Das, and E.T. Akinlabi: *Bioresour. Bioprocess*, 2024, vol. 11, p. 65.
18. J. Kivijakola, P. Rönkkö, J. Roininen, E. Erkheikki, and P. Tervonen: *Carbon Manage.*, 2025, vol. 16, p. 2574984.
19. K. Rippy, R.T. Bell, and N. Leick: *npj Mater. Sustain.*, 2024, vol. 2, p. 33.
20. R. Lundmark, E. Wetterlund, and E. Olofsson: *Biomass Bioenergy*, 2024, vol. 182, 107100.
21. L.W. Deng, Y.W. Fei, X. Liu, Z.Z. Gong, and A. Shahar: *Geochim. Cosmochim. Acta*, 2013, vol. 114, pp. 220–33.
22. A. Rafiei, N. Dogan, and S. Sun: *Metall. Mater. Trans. B*, 2026, vol. 57, p. 3859.
23. D. Djurovic, B. Hallstedt, J.V. Appenb, and R. Dronskowskib: *Calphad*, 2011, vol. 35, pp. 479–91.
24. E. Lectard, E. Hess, and R. Lin: *Metall. Res. Technol.*, 2004, vol. 101, pp. 31–38.
25. J. Cao, C. Wang, J.L. Zhang, C.K. Ji, Z.Y. Wang, and C.F. Zhang: *Ironmak. Steelmak.*, 2024, vol. 51, pp. 224–35.
26. M Reuter, Yanping Xiao, and U Boin: *VII International Conference on Molten Slags Fluxes and Salts. The South African Institute of Mining and Metallurgy*, 2004, pp 349-56.

Publisher's Note Springer Nature remains neutral with regard to jurisdictional claims in published maps and institutional affiliations.